Article

Edge-hosted Fe-N_3 sites on multiscale porous carbon framework combining high intrinsic activity with efficient mass transport for oxygen reduction

Jingjing Liu,[1] Zhichao Gong,[1] Christopher Allen,[4] Wen Ge,[2,*] Haisheng Gong,[1] Jiangwen Liao,[3] Jianbin Liu,[1] Kang Huang,[1] Minmin Yan,[1] Rui Liu,[1] Guanchao He,[1] Juncai Dong,[3] Gonglan Ye,[1,*] and Huilong Fei,[1,5*]

[1]State Key Laboratory for Chemo/Biosensing and Chemometrics, Advanced Catalytic Engineering Research Centre of the Ministry of Education, and College of Chemistry and Chemical Engineering, Hunan University, Changsha 410082, China

[2]Faculty of Materials Science and Chemistry, China University of Geosciences, Wuhan 430074, China

[3]Beijing Synchrotron Radiation Facility, Institute of High Energy Physics, Chinese Academy of Sciences, Beijing 100049, China

[4]Department of Materials, University of Oxford, Parks Road, Oxford, OX1 3PH, UK and electron Physical Science Imaging Centre, Diamond Light source Ltd., OX11 0DE, UK

[5]Lead contact

*Correspondence: gewen@cug.edu.cn; glye@hnu.edu.cn; hlfei@hnu.edu.cn

SUMMARY

Metal- and nitrogen-coordinated carbon materials (M-N/C) have emerged as the most promising nonprecious catalysts for the oxygen reduction reaction (ORR), but it remains challenging to simultaneously achieve high intrinsic activity, fast mass transport and efficient utilization of active sites in a single catalyst. Herein, we design an Fe-N/C catalyst consisting of edge-hosted Fe-N_3 sites dispersed on multiscale porous carbon frameworks (eFe-N_3/PCF). The low coordination and edge effect of the Fe-N_3 moieties endow eFe-N_3/PCF with high intrinsic activity, while the enriched nanopores enable improved mass transport and atom utilization efficiency. When evaluated by rotating disk electrode, the catalyst presents an onset potential of 1.090 V and a half-wave potential of 0.934 V *vs.* RHE in base, ranking it as one of the most active M-N/C catalysts. Further, when employed as gas diffusion electrodes, eFe-N_3/PCF displays excellent mass transport efficiency that enables high-rate and high-power capabilities at practically high current densities. This work opens up opportunities for designing high-performance ORR electrocatalysts towards applications in diverse energy conversion and storage technologies.

Keywords: edge-hosted Fe-N_3 sites; high intrinsic activity; efficient mass transport; oxygen reduction.

The bigger picture

The bigger picture statement should detail why the research is important, explain the longer-term ambitions of the research, and indicate whether the research has the potential in the short or long term to have an impact on society. The statement should be 1 or 2 paragraphs with a maximum of 1,000 characters including spaces. (For final submission, the bigger picture should be provided in a separate Word document with the eTOC blurb and highlights.)

INTRODUCTION

The oxygen reduction reaction (ORR) plays an essential role in fuel cells and metal-air batteries that are considered as two promising devices in the next-generation electrochemical energy storage (EES) systems.[1-3] Owing to the sluggish ORR kinetics, electrocatalysts are exploited to accelerate the reaction process.[4,5] Traditionally, Pt-based catalysts have been regarded as the general candidates to reduce overpotentials. However,

the scarcity and insufficient stability of commercial Pt/C largely impede its widespread applications in the EES technologies.[6-9] Therefore, it is crucial for developing Pt group metal-free (PGM-free) alternatives that combine high performance with cost-effectiveness.

Heterogeneous single-atom catalysts (SACs) are drawing tremendous attention for the 100% theoretical atom utilization efficiency, high catalytic activity and tunable electronic structure.[10-15] Among them, Fe-N/C SACs with atomically dispersed Fe-N_x sites on carbon substrate are considered as the most encouraging PGM-free ORR catalysts.[16-22] Recently, extensive research has been focused on increasing the Fe loading to obtain high-density Fe-N_x sites, but the addition of Fe in excess would cause metal atom aggregation during the pyrolysis treatment that is typically used for the preparation of Fe-N/C.[23,24] Furthermore, the utilization efficiency of Fe-N_x sites remains far below the theoretical limit as most sites are buried within the compact carbon matrix and thus have no contribution to the catalytic activity. For example, Malko *et al.* found that only 4.5% of the Fe-N_x sites in a Fe-N/C catalyst were involved in the ORR by an in situ electrochemical quantification method.[25] Therefore, it is of vital importance to improve the exposure of the Fe-N_x sites for optimizing the performance of Fe-N/C. As the ORR occurs at the triple-phase boundaries (TPBs), where O_2 and electrolyte can contact with the active sites, the creation of porous structure in Fe-N/C that can provide abundant TPBs would be effective in increasing the accessibility of the Fe-N_x sites.[5,26-28] In addition, the introduction of porous structure is particularly desirable for catalysts to be operated at high current densities (e.g., >500 mA cm^{-2}) that is usually encountered in realistic fuel-cell systems, where mass transport rather than charge transfer becomes rate limiting.[29,30] On the other hand, pore engineering could potentially generate Fe-N_x moieties with enhanced intrinsic activity. Recent experimental and theoretical studies suggested that edge-hosted Fe-N_x sites could have higher ORR activity than basal-plane-hosted counterparts due to the effects of electronic redistribution and the optimization of the intermediate binding energy.[31-34] It is expected that the creation of in-plane pores on carbon matrix would lead to the formation of abundant edge sites for hosting Fe-N_x moieties, resulting in an enhanced ORR activity. Therefore, morphology and pore engineering on the Fe-N/C catalysts are critical for the cooperative optimization of intrinsic activity, mass transport and utilization efficiency of the Fe-N_x moieties to enhance their catalytic performance, but it still remains a grand challenge.

Herein, by the combinational use of a self-assembly process and high-temperature metal etching effect, we designed a Fe-N/C ORR catalyst with edge-hosted Fe-N_3 sites dispersed on a multiscale porous carbon framework (termed as eFe-N_3/PCF) (Figure 1A). The interconnected macropores within the framework and the in-plane mesopores on the carbon nanosheets can facilitate the mass transport in the catalyst layer and at the same time increase the atom utilization efficiency (~5-fold enhancement). Additionally, the Fe-N_x sites in eFe-N_3/PCF adopt an under-coordinated Fe-N_3 configuration and preferentially orient at the edge plane, as directly visualized by atomic-scale transmission electron microscopy (TEM), due to the presence of the abundant in-plane pores. These edge-hosted Fe-N_3 sites possess enhanced intrinsic activity compared to the conventional basal-plane-hosted Fe-N_4 counterparts, demonstrated by control experiments and density functional theory (DFT) calculations. As a result, when evaluated with a rotating disk electrode (RDE) in 0.1 M KOH, eFe-N_3/PCF delivers an outstanding ORR activity with an onset potential (E_{onset}) as positive as 1.090 V (*vs.* RHE), a half-wave potential ($E_{1/2}$) of 0.934 V (*vs*. RHE) and a large kinetic current (j_k = 48.8 mA cm^{-2} at 0.8 V), superior to commercial Pt/C (E_{onset} = 0.950 V, $E_{1/2}$ = 0.845 V, j_k = 5.89 mA cm^{-2}, respectively) and almost all M-N/C ORR catalysts reported to date. Furthermore, to demonstrate the benefits of multiscale porosities in eFe-N_3/PCF for enhancing the mass transport efficiency, gas diffusion electrodes (GDEs) were fabricated and evaluated in both a three-electrode half cell and a two-electrode zinc-air battery (ZAB). Measurements show that eFe-N_3/PCF is able to deliver practically high current density in the half cell with low mass transport overpotential (e.g., 47 mV at 500 mA cm^{-2}, compared to 110 mV for the control sample) and exhibit a high peak power density of 294 mW cm^{-2} in ZAB.

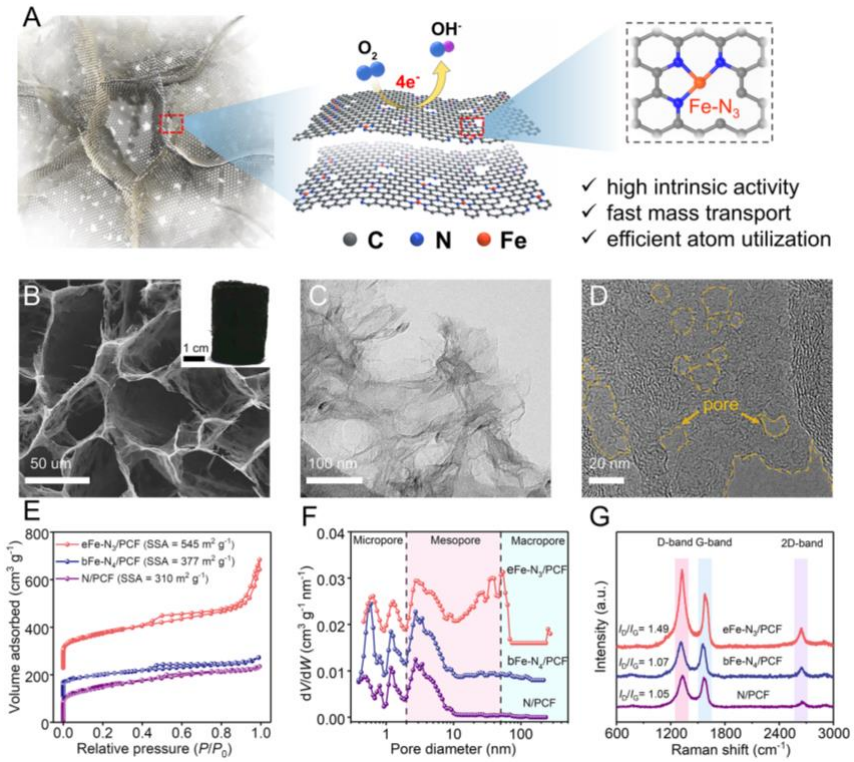

Figure 1. Characterization of morphology and porous structure

(A) Schematic illustration of the designed advantageous features of eFe-N_3/PCF for ORR catalysis.
(B) SEM image and photograph (inset) of eFe-N_3/PCF.
(C and D) TEM images at low magnification (C) and high magnification (D) of eFe-N_3/PCF.
(E and F) N_2 adsorption/desorption isotherms (E) and the corresponding pore-size distribution curves (F) of eFe-N_3/PCF, bFe-N_4/PCF and N/PCF.
(G) Raman spectra of eFe-N_3/PCF, bFe-N_4/PCF and N/PCF.

RESULTS AND DISCUSSION

Synthesis and Structural Characterization

To prepare eFe-N_3/PCF (Figure S1), a mixed solution of graphene oxide nanoribbons (GONRs) and controlled amounts of Fe precursor was firstly hydrothermally self-assembled into a hydrogel with macroporous structures. After being freeze-dried, the sample was pyrolyzed in NH_3 atmosphere to form the unsaturated and edge-hosted Fe-N_3 sites and introduce in-plane pores within the graphene nanoribbons due to the high-temperature etching effect of Fe nanoparticles (which can be washed away by post acid-leaching). The pyrolysis time was found to be important in generating the in-plane pores and thus the edge-hosted Fe-N_3 sites, as reducing the pyrolysis time failed to form the in-plane pore and accordingly a control sample consisting of basal-plane-hosted Fe-N_4 sites (denoted as bFe-N_4/PCF) can be obtained. Detailed descriptions of the preparation of eFe-N_3/PCF, bFe-N_4/PCF and other control samples were provided in the Supplemental Information.

The morphology and pore structure of eFe-N_3/PCF were firstly characterized by various techniques, as shown in Figure 1. Scanning electron microscopy (SEM) image reveals the interconnected three-dimensional macroporous carbon framework of eFe-N_3/PCF (Figure 1B), and the inset shows the optical image of the monolithic aerogel. TEM image displays that the graphene nanoribbons are entangled with each other (Figure 1C). Further, the high-resolution TEM (HR-TEM) image reveals numerous mesopores in the size range of ~10-50 nm that could improve mass transfer and provide abundant edge sites for hosting Fe-N_3 moieties (Figure 1D). Nitrogen adsorption and desorption analysis in Figure 1E shows that eFe-N_3/PCF displays a classic type IV isotherm with an apparent hysteresis loop at moderate pressure, indicating the existence of ample mesopores.[35-38] Brunauer-Emmett-Teller (BET)

surface area analysis shows that the specific surface area (SSA) of eFe-N_3/PCF (545 m^2 g^{-1}) is significantly higher than that (377 m^2 g^{-1}) of bFe-N_4/PCF and that (310 m^2 g^{-1}) of N/PCF (prepared by a similar method to eFe-N_3/PCF but without the addition of metal precursor). The pore size distribution curves suggest that eFe-N_3/PCF is mainly enriched with ~10-70 nm nanopores and it has a significantly increased total mesopore volume of 0.386 cm^3 g^{-1} compared to that (0.190 cm^3 g^{-1}) of bFe-N_4/PCF and that (0.151 cm^3 g^{-1}) of N/PCF (Figures 1F and S2, and Table S1). It is noted that other than the pyrolysis time period, the amounts of Fe precursor added during preparation can be used to effectively tune the porosity of the catalysts (Figures S3-S4 and Table S2). Figure 1G shows the Raman spectra with the presence of the defect-related D-band at 1335 cm^{-1} and graphitic carbon-related G-band at 1580 cm^{-1}.[39-41] A higher I_D-to-I_G ratio of eFe-N_3/PCF (1.49) than that (1.07) of bFe-N_4/PCF and that (1.05) of N/PCF suggests its higher degree of defects due to the presence of abundant in-plane holes and edge sites. The surface wetting property of the catalysts was studied by water contact angle (CA) measurements. As shown in Figure S5, the water CA of eFe-N_3/PCF (~135°) is larger than that (~121°) of bFe-N_4/PCF, suggesting its enhanced hydrophobicity. The multiscale porosity and hydrophobicity of eFe-N_3/PCF could benefit the transport of gaseous O2 reactants during the ORR process.

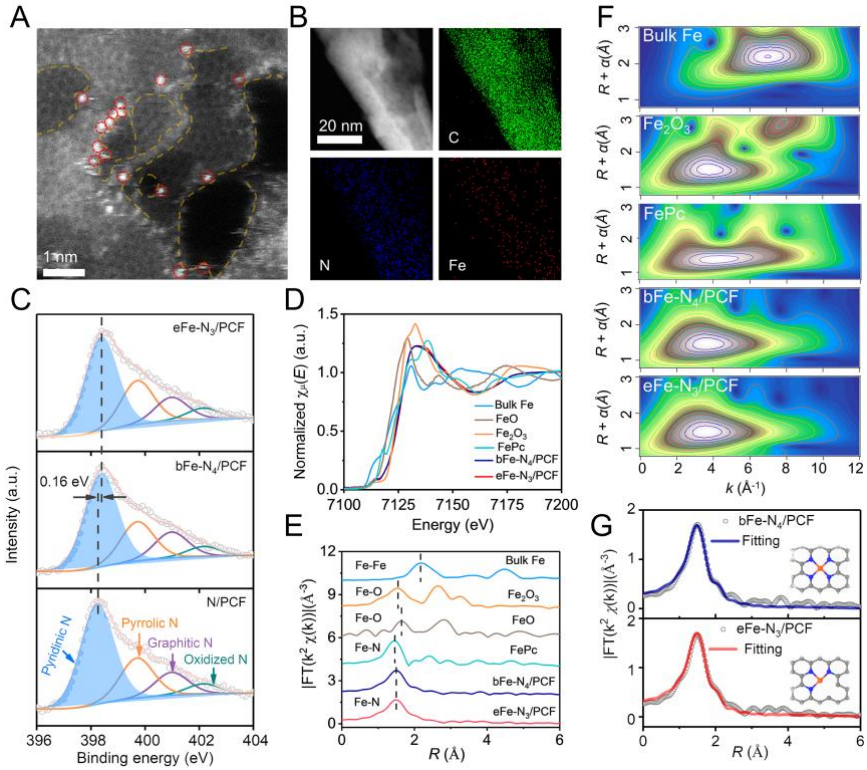

Figure 2. Analysis of composition and atomic structure

(A) ADF-STEM image of eFe-N_3/PCF. The Fe atoms are marked by the red circles, and the pore edges of graphene are marked by the orange dashed lines.
(B) TEM image and corresponding elemental mapping images of eFe-N_3/PCF.
(C) The high-resolution N 1s XPS spectra of eFe-N_3/PCF, bFe-N_4/PCF and N/PCF.
(D and E) The Fe K-edge XANES (D) and FT k^2-weighted EXAFS (E) spectra of eFe-N_3/PCF, bFe-N_4/PCF and the reference samples of bulk Fe, FeO, Fe_2O_3 and FePc.
(F) Wavelet transforms for the k^2-weighted Fe K-edge EXAFS signals of eFe-N_3/PCF, bFe-N_4/PCF and the reference samples of bulk Fe, Fe_2O_3 and FePc.
(G) Comparisons between experimental FT-EXAFS spectra and fitting curves of eFe-N_3/PCF and bFe-N_4/PCF.

Analysis of composition and atomic structure

The annular dark-field scanning TEM (ADF-STEM) shows that the Fe metals in eFe-N_3/PCF are atomically dispersed on the carbon substrate and preferably situate at the defective edge sites (Figure 2A and Figure S6). No Fe nanoparticles were detected by X-ray diffraction (XRD)

(Figure S7). The Fe loading in eFe-N_3/PCF and bFe-N_4/PCF was determined to be 0.73 wt% and 0.71 wt%, respectively, by inductively coupled plasma mass spectrometry (ICP-MS) (Table S3). Energy dispersive X-ray spectroscopy (EDX) mapping images reveal that C, N and Fe elements distribute uniformly over the graphene nanoribbons in eFe-N_3/PCF (Figure 2B). The X-ray photoelectron spectroscopy (XPS) survey spectra demonstrate eFe-N_3/PCF has a higher N content (3.19 at%) than N/PCF (2.62 at%) and bFe-N_4/PCF (2.93 at%) (Figure S8 and Table S4), possibly attributing to its edge abundancy for N doping. High-resolution N1s XPS spectra of these three catalysts were fitted into four peaks that can be assigned to pyridinic N, pyrrolic N, graphitic N, and oxidized N (Figure 2C).[11,42] Notably, the peak positions for the pyridinic N of eFe-N_3/PCF and bFe-N_4/PCF shift positively (~0.16 eV) compared to N/PCF, indicating the formation of Fe-pyridinic N bond.[43]

To further probe the atomistic and electronic structure of Fe sites, X-ray absorption near-edge structure (XANES) and extended X-ray absorption fine structure (EXAFS) analyses were performed. As shown in Figure 2D, the Fe K-edge adsorption energy of eFe-N_3/PCF and bFe-N_4/PCF situates between FeO and Fe_2O_3 reference compounds, suggesting the oxidation state of Fe is between +2 and +3. The Fourier-transformed EXAFS (FT-EXAFS) spectra of eFe-N_3/PCF and bFe-N_4/PCF both exhibit a main peak situated at ~1.5 Å in *R* space (Figure 2E), close to the main peak of the iron phthalocyanine (FePc) reference, which can be assigned to the Fe-N instead of Fe-Fe bond (2.2 Å). Furthermore, the EXAFS wavelet transforms (WT) analyses demonstrate only one maximum intensity at ~4.0 $Å^{-1}$ in *k* space (Figure 2F), confirming that the Fe metals exist as mononuclear Fe centre with Fe-N coordination in eFe-N_3/PCF and bFe-N_4/PCF.[12,44,45] Quantitative structural parameters were extracted by least-squares EXAFS curve-fitting analyses (Figures 2G and S9 and Table S5), suggesting that the average number of N coordinators in the first coordination shell of Fe is 3.0 and 4.0 at Fe-N distances of 1.89 Å and 1.96 Å for eFe-N_3/PCF and bFe-N_4/PCF, respectively. From the above structural analyses, it is determined that the single Fe atoms in eFe-N_3/PCF adopt under-coordinated and edge-hosted Fe-N_3 moieties, in contrast to the basal-plane-hosted Fe-N_4 moieties in bFe-N_4/PCF.

ORR Performance Evaluated by RDE technique

The ORR activities of the catalysts were first assessed by RDE technique with a typical three-electrode system in 0.1 M KOH. The potential of the reference electrode was calibrated with respect to the reversible hydrogen electrode (RHE) (Figure S10), and all potentials obtained by RDE test were corrected with 95% *iR*-compensation unless otherwise specified. It is noted that the ORR activity has been optimized by adjusting the amounts of Fe precursor (Figure S11). From the cyclic voltammetry (CV) curves, eFe-N_3/PCF demonstrates an obvious O_2 reduction peak and highest cathodic peak current density in O_2-saturated electrolyte compared to control samples due to its high intrinsic activity and improved mass transport (Figure S12). From the linear sweep voltammetry (LSV) measurements (Figure 3A), eFe-N_3/PCF delivers the highest ORR activity with an early onset potential (E_{onset}, defined as the potential at 0.1 mA cm^{-2}) of 1.090 V and a half-wave potential ($E_{1/2}$) of 0.934 V, which are much higher than N/PCF (0.863 V and 0.734 V), bFe-N_4/PCF (1.050 V and 0.830 V) as well as Pt/C (0.950 V and 0.845 V), and even superior to almost all Fe or other M-N/C-based SACs reported so far (Figure 3B and Table S6). Additionally, eFe-N_3/PCF presents a kinetic current density (j_K) of 48.8 and 7.62 mA cm^{-2} at 0.8 and 0.85 V, respectively, much higher than N/PCF (1.60 mA cm^{-2} and 0.557 mA cm^{-2}), bFe-N_4/PCF (4.12 mA cm^{-2} and 2.27 mA cm^{-2}) and Pt/C (5.89 mA cm^{-2} and 4.30 mA cm^{-2}) (Figure 3C). Meanwhile, eFe-N_3/PCF possesses a lower Tafel slope of 60.1 mV dec^{-1} than bFe-N_4/PCF (171.2 mV dec^{-1}) (Figure S13), highlighting the faster ORR kinetics of eFe-N_3/PCF. The electron transfer number (*n*) was determined to be close to 4 and the generated H_2O_2 yield is negligible (~3%) for eFe-N_3/PCF in 0.2-0.8 V measured by rotating ring disk electrode (RRDE) (Figure 3D), suggesting a desired Pt-like 4-electron ORR pathway, in accordance with those derived from Koutecký-Levich (K-L) linear plots (Figure S14). In comparison, the control samples of N/PCF and bFe-N_4/PCF show inferior selectivity towards the 4-electron pathway. Additionally, eFe-N_3/PCF exhibits a current retention of 97.4% after 12 h chronoamperometry test, and there was only 8 mV degradation of $E_{1/2}$ after 10000 CV cycles (Figure S15), revealing the excellent stability of eFe-N_3/PCF. Furthermore, eFe-N_3/PCF shows a superior methanol resistance (Figure S16). The ORR performance of eFe-N_3/PCF was also evaluated in 0.1 M $HClO_4$ and 0.1 M PBS, suggesting that it could be a potential pH-universal ORR catalyst candidate (Figures S17 and S18).

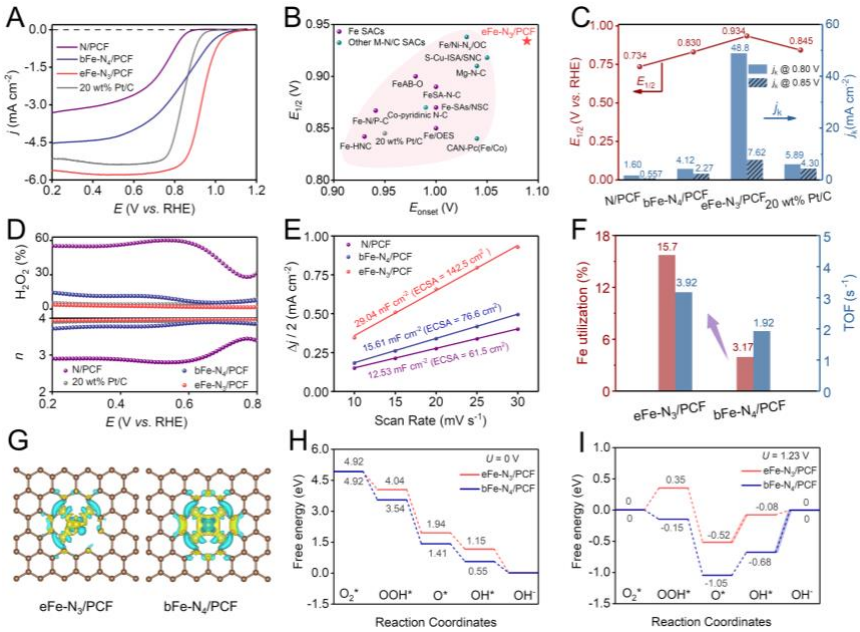

Figure 3. Electrocatalytic performance toward ORR of the catalysts evaluated with RDE technique

(A) LSV curves of N/PCF, eFe-N_3/PCF, bFe-N_4/PCF and Pt/C in 0.1 M KOH.
(B) Comparison of ORR activities in terms of E_{onset} and $E_{1/2}$ between eFe-N_3/PCF and the state-of-the-art Fe or other M-N/C-based SACs reported recently.
(C) Comparison of $E_{1/2}$ and j_k at 0.8 V and 0.85 V *vs.* RHE for N/PCF, eFe-N_3/PCF, bFe-N_4/PCF and Pt/C.
(D) H_2O_2 yield and electron transfer number (n) of the corresponding catalysts.
(E) The electrochemical double-layer capacitance C_{dl} and ECSA of N/PCF, eFe-N_3/PCF and bFe-N_4/PCF.
(F) Comparison of Fe utilization efficiency and TOF between eFe-N_3/PCF and bFe-N_4/PCF.
(G) Calculated charge densities difference of eFe-N_3/PCF and bFe-N_4/PCF (blue and yellow regions represent electron depletion and electron accumulation, respectively).
(H and I) Free energy diagrams of the ORR on the two models at 0 V (H) and 1.23 V (I) *vs.* RHE, respectively.

The exceptional ORR activity of eFe-N_3/PCF can be partially ascribed to its multiscale porous structure, which can promote the electrochemical active surface area (ECSA) and accessibility of the active sites. On the basis of electrochemical double-layer capacitance (C_{dl}) tested at the non-Faradaic potential region,[46,47] the ECSA of eFe-N_3/PCF was estimated to be 142.5 cm^2, much higher than bFe-N_4/PCF (76.6 cm^2) and N/PCF (61.5 cm^2) (Figures 3E and S19). To quantify the utilization efficiency of the Fe-N_x moieties in eFe-N_3/PCF and bFe-N_4/PCF, in situ nitrate adsorption and reductive stripping experiments were carried out (Figure S20).[25,48] As summarized in Figure 3F, the Fe utilization efficiency of eFe-N_3/PCF is 15.70%, which is about five times as high as bFe-N_4/PCF (3.17%), suggesting the critical role of porosity in exposing active sites. Besides, the high ORR performance of eFe-N_3/PCF can be additionally attributed to the high intrinsic activity of the edge-hosted and low-coordinated Fe-N_3 moieties. The ECSA-normalized j_k shows that eFe-N_3/PCF delivers higher values than bFe-N_4/PCF, suggesting that eFe-N_3/PCF has a higher intrinsic activity (Figure S21). The turnover frequency (TOF) value, which manifests the intrinsic activity on the per-site basis,[49] was estimated to be 3.92 s^{-1} for eFe-N_3/PCF at 0.8 V that is much higher than the value of 1.92 s^{-1} for bFe-N_4/PCF. To further elucidate the origin for the high intrinsic activity of eFe-N_3/PCF, DFT calculation was conducted to investigate the free energetics of ORR-related mechanism. As shown in Figure 3G, the edge-hosted Fe-N_3 moieties display increased electron density (yellow region) around the Fe atom than the basal-plane-hosted Fe-N_4 sites, revealing the charge density re-distribution on eFe-N_3/PCF due to the low coordination of the edge-sited Fe.[32,50] The typical 4e^- transfer ORR processes with the optimized atomic configurations for eFe-N_3/PCF and bFe-N_4/PCF were illustrated in Figure S22, and the corresponding Gibbs free energy diagrams at U = 0 V and U = 1.23 V (*vs.* RHE)

were shown in Figure 3H and Figure 3I, respectively. All elementary steps for the two catalysts at U = 0 V are thermodynamically downhill, suggesting that the process is exothermic and favorable under this potential (Figure 3H and Table S7). In contrast, at U = 1.23 V (Figure 3I), eFe-N_3/PCF reveals an energy barrier of 0.44 eV at the rate-determining step ($O^* + H_2O + e^- \rightarrow OH^* + OH^-$), lower than bFe-$N_4$/PCF (0.68 eV) at the rate-determining step ($OH^* + e^- \rightarrow OH^- + *$). Accordingly, the estimated ORR onset potential of eFe-N_3/PCF (0.79 V) is higher than bFe-N_4/PCF (0.55 V) (Figures S23 and S24), confirming the higher intrinsic activity of eFe-N_3/PCF. In brief, the DFT calculation results show that the edge-hosted Fe-N_3 moieties could optimize the electronic structure and lower the ORR overpotentials.

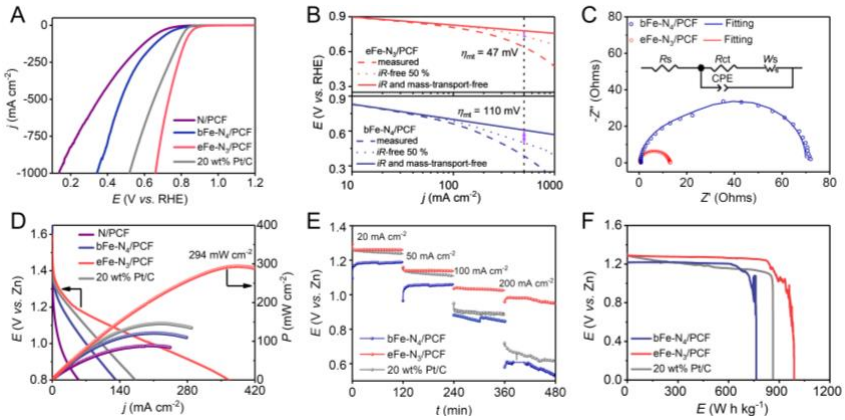

Figure 4. Electrocatalytic performance toward ORR of the catalysts evaluated with GDEs in a three-electrode half cell configuration and two-electrode ZAB

(A) ORR LSV polarization curves in 1.0 M KOH at 10 mV s^{-1} for N/PCF, eFe-N_3/PCF, bFe-N_4/PCF and Pt/C with GDEs.

(B) Determination of the mass-transport overpotentials (η_{mt}) of eFe-N_3/PCF and bFe-N_4/PCF.

(C) Nyquist plots for GDEs of the cathode catalysts at 0.85 V (inset is the equivalent circuit model). Z' and Z'' are the real and imaginary parts of the impedance.

(D) The discharge polarization curves and the corresponding power densities of N/PCF, eFe-N_3/PCF, bFe-N_4/PCF and Pt/C in ZABs.

(E) The discharge platforms of eFe-N_3/PCF, bFe-N_4/PCF and Pt/C at various current densities in ZABs.

(F) The energy densities plots of eFe-N_3/PCF, bFe-N_4/PCF and Pt/C in ZABs.

ORR Performance Evaluated by GDEs configuration

The electrocatalytic performance of the catalysts was further investigated by GDE half cells, which offer several advantages over thin film RDE measurements with negligible mass transport limitations and for fast catalyst evaluation under practical operation conditions of fuel cells.[51,52] The testing configuration and device for the GDE half cells were shown in Figure S25. From the polarization curves in Figure 4A and Figures S26-S27, eFe-N_3/PCF with an optimized loading of 0.8 mg cm^{-2} exhibits considerably high ORR activity at high current densities up to 1000 mA cm^{-2} with much smaller overpotentials than bFe-N_4/PCF, N/PCF and Pt/C, attributing to its enhanced mass transfer efficiency. To compare the mass transfer efficiency of eFe-N_3/PCF and bFe-N_4/PCF, the mass-transport overpotentials (η_{mt}) at high current densities were extracted from the polarization curves (Figure 4B), showing that eFe-N_3/PCF exhibits a η_{mt} of 47 mV at 500 mA cm^{-2}, which is much smaller than that (110 mV) of bFe-N_4/PCF. Nyquist plots of electrochemical impedance spectroscopy simulated by the Randles equivalent circuit model reveals that only one arc is observed for eFe-N_3/PCF, suggesting that the ORR process is mainly kinetically controlled. In contrast, an obvious and additional arc at low frequency shows up for bFe-N_4/PCF, indicative of considerable mass transport limitations (Figure 4C and Figure S28, Table S8).[16,53] In addition, the long-term stability of eFe-N_3/PCF was assessed with the GDE configuration by chronopotentiometry measurement at 100 mA cm^{-2} for 100 h and CV cycling for 5000 cycles, which both show negligible change in potential (Figures S29 and S30), indicating its robust catalytic stability. The XRD pattern and ADF-STEM image of eFe-N_3/PCF collected after the durability test suggested no aggregation of Fe nanoparticles and that the Fe metals maintained atomic dispersion on the carbon substrate (Figures S31 and S32), revealing the excellent structural stability of eFe-N_3/PCF. Moreover, when GDE was used as the air cathode in a ZAB, eFe-

N_3/PCF exhibits an open circuit potential of 1.58 V *vs.* Zn, which is much higher than other control samples (Figure S33). From the LSV polarization curves and discharge curves at various current densities (20, 50, 100 and 200 mA cm^{-2}) (Figures 4D and 4E), eFe-N_3/PCF presents lower overpotentials than bFe-N_4/PCF, N/PCF and Pt/C at all current densities and the performance differences become more pronounced at higher current densities, highlighting the importance of multiscale porous structures of eFe-N_3/PCF in enhancing its mass transport and thus enabling high-rate capability. Moreover, eFe-N_3/PCF displays a maximum power density of 294 mW cm^{-2} at 385 mA cm^{-2} and an energy density of 988 Wh kg_{Zn}^{-1}, much outperforming commercial Pt/C (146 mW cm^{-2} at 224 mA cm^{-2}, 863 Wh kg_{Zn}^{-1}) and bFe-N_4/PCF (122 mW cm^{-2} at 211 mA cm^{-2}, 764 Wh kg_{Zn}^{-1}) (Figure 4F). Overall, the GDE measurements in both three-electrode half cell and two-electrode ZAB demonstrate the efficient mass transport and high-rate/power capability of eFe-N_3/PCF.

Conclusion

In conclusion, by morphology and pore engineering, we designed a multiscale porous eFe-N_3/PCF catalyst that has combined merits of high intrinsic activity originated from the under-coordinated and edge-hosted Fe-N_3 moieties, improved utilization of active sites and mass transport efficiency as a result of the macropores within the three-dimensional carbon framework and the in-plane mesopores in the graphene nanosheets. Benefiting from these advantageous features, eFe-N_3/PCF exhibits an exceptional catalytic activity toward ORR with an onset potential of 1.090 V and a half-wave potential of 0.934 V *vs.* RHE, outperforming Pt/C and almost all state-of-the-art M-N/C SACs. Additionally, when employed as GDEs, eFe-N_3/PCF could deliver high current densities up to 1000 mA cm^{-2} at relatively low overpotentials in a half cell configuration and a high peak power density of 294 mW cm^{-2} in a ZAB. It is convinced that the results presented in this work would guide the rational design and synthesis of prominent SACs for basic research and practical applications.

EXPERIMENTAL PROCEDURES

Resource availability

Lead contact

Further information and requests for resources should be directed to and will be fulfilled by the lead contact, Huilong Fei (hlfei@hnu.edu.cn).

Materials availability

This study did not generate new unique reagents. All the chemical materials and experimental procedures are summarized in the following.

Data and code availability

Full experimental procedures and experimental data are provided in the supplemental information.

Reagents and Chemicals

Multi-walled carbon nanotubes (MWCNTs) were purchased from Chengdu Organic Chemicals Co. Ltd. (outer diameter: 30~80 nm, >99.9 wt%). Concentrated sulfuric acid (H_2SO_4, 98.3%), hydrochloric acid (HCl, 36~38%), phosphoric acid (H_3PO_4, 85%), and potassium permanganate ($KMnO_4$, 99.5%) were purchased from Sinopharm Chemical Reagent Co., Ltd. Iron (III) chloride hexahydrate ($FeCl_3 \cdot 6H_2O$, >99%) was purchased from GENERAL-REAGENT. Potassium hydroxide (KOH, >90%) and sodium nitrite ($NaNO_2$) were brought from Shanghai Macklin Biochemical Co., Ltd. Nafion 117 solution (5 wt%) was brought from Sigma-Aldrich. Carbon fiber paper (CFP) (HCP120) was purchased from Shanghai Hesen. All of these chemicals were used as received without any further purification.

Synthesis of graphene oxide nanoribbons (GONRs)

GONRs were prepared from multiwalled carbon nanotubes (MWCNTs) via oxidative unzipping that was reported previously.[54] In brief, 150 mg of MWCNTs were firstly suspended in 36 mL H_2SO_4 by stirring the mixture for 1 h at room temperature. Secondly, H_3PO_4 (4 mL) was then added and the mixture was stirred for another 15 min before the addition of $KMnO_4$ (750 mg). It should be careful to add $KMnO_4$ in batches to prevent explosion. Thirdly, the reaction mixture was heated at 65 °C for 2 h and then allowed to cool to room temperature. Finally, the aforementioned reaction mixture was poured onto 100 mL of ice containing H_2O_2

(30%, 5 mL) and then the resulting light-brown colored precipitate was centrifuged until pH~7. The collected GONRs were diluted to 2 mg ml^{-1} for further use.

Synthesis of eFe-N_3/PCF

The synthesis route of eFe-N_3/PCF is diagrammed in Figure S1. Specifically, 175 uL $FeCl_3$•$6H_2O$ (3.4 mg mL^{-1}) was added to 8 mL (2 mg mL^{-1}) GONRs, and the mixture was sonicated for 30 min and stirred for 20 min. Then, the well-mixed dispersion was transferred into a 50 mL polytetrafluoroethylene (PTFE) reactor to conduct the hydrothermal reaction at 120 °C for 12 h, resulting in the formation of a 3D porous hydrogel. After being lyophilized, the gel was pyrolyzed at 800 °C for 1.5 h in a tubular furnace under a constant flow of Ar/NH_3 (150/50 sccm) with a heating rate of 22.5 °C min^{-1}. This step would induce the formation of atomically dispersed Fe sites as well as Fe nanoparticles, which were responsible for the generation of the in-plane holes in the graphene nanoribbons due to the high-temperature Fe etching effect. To wash away the excessive Fe nanoparticles, the pyrolyzed sample was acid-leached with 0.5 M H_2SO_4. A second calcination (800 °C, 10 min) was carried out to obtain the final product of eFe-N_3/PCF. For comparison, control sample of bFe-N_4/PCF was prepared following the same procedure of eFe-N_3/PCF but reducing the first-step pyrolysis time down to 0.5 h to minimize the etching of carbon matrix by the Fe nanoparticles. Another control sample of N/PCF was prepared without the addition of Fe precursor. Further, the amounts of Fe salts added in the precursor were varied to optimize the FeN_x sites density and porosity in the catalysts (labeled as Fe-N/PCF-*X*, *X* = 0.1, 1 and 1.2, representing that the added amounts of Fe salts were 17.5 uL, 175 uL and 210 uL, respectively).

Rotating disk electrode (RDE) and rotating ring disk electrode (RRDE) tests

All the electrochemical measurements were performed in 0.1 M KOH on a CHI 760E electrochemical workstation (Chenhua, Shanghai, China) with a traditional three-electrode system with glassy carbon electrode (5 mm in diameter), Hg/HgO electrode and graphite rod as the working electrode, reference electrode and counter electrode, respectively. To prepare the working electrodes, 2 mg electrocatalyst was added into the mixture of 960 uL of alcohol and 40 uL of Nafion (5 wt%). After sonicating for 60 min, 10 μL of the suspension was dropped on a glassy carbon electrode for tests (0.101 mg cm^{-2}; 0.203 mg cm^{-2} for bFe-N_4/PCF). For comparison, an electrode based on Pt/C (20 wt%) (0.101 mg cm^{-2}) catalyst ink was prepared with the similar protocol. Cyclic voltammetry (CV) curves were tested in 0~1.2 V *vs*. RHE with a scan rate of 50 mV s^{-1}. The linear sweep voltammetry (LSV) measurements were performed by RDE and RRDE (Pine Research Instrumentation) at the rotating speed varied from 400 to 1600 rpm with a scan rate of 10 mV s^{-1} in O_2-saturated 0.1 M KOH. All LSV curves were corrected with background current with those collected in N_2-saturated 0.1 M KOH. The electrochemical double layer capacitance (C_{dl}) was derived from CV curves at non-Faradaic region (from 1.10 V to 1.20 V *vs.* RHE) at various scan rates of 10, 15, 20, 25 and 30 mV s^{-1}. The methanol tolerance was studied by the chronoamperometry measurement in 0.1 M KOH mixed with 3 M methanol as electrolyte. All potentials derived by RDE test in 0.1 M KOH were converted to the reversible hydrogen electrode (RHE) potentials by $E_{RHE} = E_{Hg/HgO} + 0.903$ based on the calibration results (Figure S10), and corrected with 95% *iR*-compensation.

To probe the ORR kinetics, Koutecký-Levich (K-L) plots were obtained from the following equations:

$$\frac{1}{j} = \frac{1}{j_L} + \frac{1}{j_k} = \frac{1}{B\omega^{\frac{1}{2}}} + \frac{1}{j_k} \qquad \text{(Equation 1)}$$

$$B = 0.62nFC_0(D_0)^{2/3}v^{-1/6} \qquad \text{(Equation 2)}$$

where j is the measured current density; j_L and j_k are the diffusion-limited current density and kinetic current density, respectively; ω is the angular velocity; n is transferred electron number; F is Faraday constant (96485 C mol^{-1}); C_o is the bulk concentration of O_2 (1.15×10^{-6} mol cm^{-3}); D_o is the diffusion coefficient of O_2 in 0.1 M KOH (1.9×10^{-5} cm^2 s^{-1}); v is the kinetic viscosity of the electrolyte (0.01 cm^2 s^{-1}).

The electron transfer number (n) and hydrogen peroxide yield (H_2O_2%) were evaluated by the following two equations with RRDE tests:

$$H_2O_2\% = 200 \times \frac{\frac{I_R}{N}}{\frac{I_R}{N} + I_D} \qquad \text{(Equation 3)}$$

$$n = 4\times \frac{I_D}{I_D+\frac{I_R}{N}} \quad \text{(Equation 4)}$$

where I_R and I_D are the ring and disk currents. N is the ring current collection efficiency which was calibrated to be 23.7% (Figure S34).

Quantification of the number of the active site density (SD)

The number of active site density (SD) and turnover frequency (TOF) were quantified according to the technique presented by Malko *et al.* by RDE setup in 0.5 M acetate buffer electrolyte with pH = 5.2.[16,25] The principle is based on the observation that nitrite (NO_2^-) can interact with the Fe sites in the Fe-N/C catalyst and the electrochemical measurements consist of five steps: experimental cleaning protocol (-0.4~1.05 V *vs.* RHE), measurement (un-poisoned; 0.3~1.0V *vs.* RHE), electrode poisoning (-0.3~0.4 V *vs.* RHE), measurement (poisoned and strip; 0.3~1.0 V *vs.* RHE and -0.3~0.4 V *vs.* RHE) and measurement (recovered; -0.3~0.4 V *vs.* RHE and 0.3~1.0 V *vs.* RHE, repeatedly). All the aforementioned electrochemical tests were operated on a traditional three-electrode system. Specifically, glassy carbon electrode, calomel electrode and graphite rod were used as the working electrode, reference electrode and counter electrode, respectively. The corresponding ORR performance was recorded before, during and after the NO_2^- absorption. The excess nitrosyl reduction charge (Q_{strip}) associated with the stripping peak was proportional to the SD, and TOF was calculated by dividing the difference of kinetic current density between the poisoned and the un-poisoned state of eFe-N_3/PCF at 0.8 V. All the potentials were converted to the reversible hydrogen electrode (RHE) potentials by $E_{RHE} = E_{Hg/Hg_2Cl_2} + 0.538$ based on the calibration results in 0.5 M acetate buffer (Figure S35). The SD and TOF values were calculated by the following two equations:

$$\text{SD (mol g}^{-1}) = \frac{Q_{strip}\,(\text{C g}^{-1})}{n_{strip}F\,(\text{C mol}^{-1})} \quad \text{(Equation 5)}$$

$$\text{TOF (s}^{-1}) = \frac{n_{strip}\,\Delta j_k\,(\text{mA cm}^{-2})}{Q_{strip}\,(\text{C g}^{-1})Lc(\text{mg cm}^{-2})} \quad \text{(Equation 6)}$$

where Q_{strip} is the excess coulometric charge associated with the stripping peak; n_{strip} is the number of electrons associated with the reduction of one adsorbed nitrosyl per site (n = 5); F is the Faraday constant (96485 C mol^{-1}); $j_k = \frac{j_{lim}\times j}{j_{lim}-j}$ (mA cm^{-2}) is the kinetic current density (0.8 V *vs.* RHE); Lc is the catalyst loading.

Gas diffusion electrode (GDE) half cell test

A gas diffusion electrode (GDE) electrochemical half cell with negligible mass transport limitations was developed to simulate the real fuel cell test conditions.[51,52] The GDE electrochemical test was measured on a three-electrode system with the GDE as the working electrode, a graphite rod as the counter electrode and Hg/HgO reference electrode in 1 M KOH (Figure S25). To prepare the GDE, catalysts ink consisting of 4 mg electrocatalysts, 960 uL alcohol and 40 uL Nafion (5 wt%) were drop-casted on gas diffusion CFP (HCP120) and dried at 60 °C for 4 h. All the loadings of prepared catalysts and commercial Pt/C was 0.8 mg cm^{-2}. Electrochemical impedance spectroscopy (EIS) was tested between 0.01~1000000 Hz (quiet time: 2 s; AC excitation amplitude: 5 mV). All the potentials were converted to the reversible hydrogen electrode (RHE) potentials by $E_{RHE} = E_{Hg/HgO} + 0.918$ based on the calibration results in 1.0 M KOH (Figure S36), and all potentials were corrected with 50% *iR*-compensation.

Zn-air battery test

A home-made primary Zn-air battery was assembled with catalysts-coated GDE as the air electrode, Zn plate (thickness: 0.5 mm; purity: 99.99%) as the counter electrode and 6 M KOH as the electrolyte. The air electrode was prepared by uniformly coating the as-fabricated catalysts ink onto CFP (HCP120) and then dried at 60 °C for 4 h. The catalysts loadings were 0.8 mg cm^{-2} (Pt/C: 0.4 mg cm^{-2}). The discharge polarization curves of the battery were operated at a sweep rate of 10 mV s^{-1}. The power density (P) and energy density (E) were calculated as follows:

$$P = IV \quad \text{(Equation 7)}$$

where I is the discharge current density and V is the corresponding voltage.

$$E = \frac{VIt}{m_{Zn}} \quad \text{(Equation 8)}$$

where V is the average voltage, I is the discharge current density, t is the discharge time, m_{Zn} is the consumed weight of Zn.

Density functional theory calculation (DFT)

All the density functional theory calculations were performed using the Vienna *Ab Initio* Simulation Program (VASP).[55,56] The generalized gradient approximation (GGA) in the Perdew-Burke-Ernzerhof (PBE) form and a cutoff energy of 500 eV for planewave basis set was adopted.[57] A 5 × 5 × 1 Monkhorst-Pack[58] grid was used for sampling the Brillouin zones at structure optimization, whereas a denser mesh of 11 × 11 × 1 was used for the electronic structure calculations. The ion-electron interactions were described by the projector augmented wave (PAW) method.[59] The supercell containing a 5 × 3 periodic rectangular graphene sheets (60C atoms) was used to build the Fe-N/C systems. Sufficient vacuum of 20 Å has been considered to avoid periodic interaction. A DFT-D3 semiempirical correction was described via Grimme's scheme method.[57] The convergence criteria of structure optimization were chosen as the maximum force on each atom less than 0.02 eV/Å with an energy change less than 1×10^{-5} eV.

The ORR process (the pH is set to 13 in this study) can be described as:

$$O_2\,(g) + 2H_2O\,(l) + 4e^- \rightarrow 4OH^- \qquad \text{(Equation 9)}$$

The four electron reaction steps are as followed:

$$* + O_2\,(g) \rightarrow O_2* \qquad \text{(Equation 10)}$$

$$O_2*(g) + H_2O\,(l) + e^- \rightarrow OOH* + OH^- \qquad \text{(Equation 11)}$$

$$OOH* + e^- \rightarrow O* + OH^- \qquad \text{(Equation 12)}$$

$$O* + H_2O + e^- \rightarrow OH* + OH^- \qquad \text{(Equation 13)}$$

$$OH* + e^- \rightarrow OH^- + * \qquad \text{(Equation 14)}$$

the * represents the substrate, (l) and (g) denote the liquid and gas phases, respectively.

The Gibbs free energy change (ΔG) for each elemental step is defined as:[60,61]

$$\Delta G = \Delta E + \Delta ZPE - T\Delta S + \Delta G_U + \Delta G_{pH} \qquad \text{(Equation 15)}$$

where ΔE is obtained directly from DFT calculations, ΔZPE is the change of zero-point energies (ZPE), T is temperature that refers to room temperature (T = 298.15 K), ΔS is the change in entropy, ΔG_U is the contribution of electrode potential to ΔG, and it is computed on the basis of the assumption that the chemical potential of a proton/electron ($H^+ + e^-$) in solution is equal to half of the chemical potential of a gaseous H_2 and shifting ΔG by $-eU$ in each proton/electron transfer step, where e is the number of electrons transferred and U is the applied electrode potential. The ZPE and entropies of ORR intermediates are calculated from the vibrational frequencies, and those of gas-phase molecules are obtained from the standard thermodynamic database. The free energy of O_2 was obtained from the reaction $2H_2O \rightarrow O_2 + 2H_2$ for which the free energy change is 4.92 eV. The overpotential for ORR (η^{ORR}) is calculated by:[62]

$$\eta^{ORR} = 1.23 + \max\{\Delta G_a, \Delta G_b, \Delta G_c, \Delta G_d\}/e \qquad \text{(Equation 16)}$$

Material characterization

Field-emission scanning electron microscope (SEM) (FEI Quanta 250), and transmission electron microscope (TEM) (FEI Titan G2 60-300) were used to study the morphology of the catalysts. The annular dark-field scanning TEM (ADF-STEM) was performed on JEOL ARM300 CF with JEOL ETA aberration correctors with beam energy 80 keV, 40 um condenser lens aperture (32mrad), ADF detector (inner angle 47mrad) and beam current approx. 46 pA. The X-ray powder diffractometer (XRD) (Bruker/AXS D8 Advance, Cu Kα radiation, λ = 1.5406 Å, 40 kV and 40 mA), XPS (Kratos AXIS SUPRA, Al Kα radiation) and Raman (Via-reflex, 532 nm) were employed to investigate the structure and composition of these catalysts.

Inductively coupled plasma mass spectrometry (ICP-MS) (Agilent 7900) was used to detect the metal content. The pore and morphological features of the various catalysts were determined by nitrogen physisorption at 77 K in a Micromeritics ASAP 2460. The Fe K-edge X-ray absorption spectra (XAS) were performed at beamline 1W1B in fluorescence mode by using a Si (111) double-crystal monochromator (Beijing Synchrotron Radiation Facility). A detuning of about 25% by misaligning the Si (111) crystal was performed to minimize the higher harmonics. The storage ring of BSRF was operated at 2.5 GeV with a maximum current of 250 mA in decay mode. The incident and fluorescence X-ray intensities were monitored by using standard N_2-filled ionization chambers and Ar-filled Lytle-type detector, respectively. An energy calibration was conducted using reference bulk Fe. The raw data were background subtracted, normalized, Fourier transformed and fitted by using the Demeter software.

SUPPLEMENTAL INFORMATION

This section includes supplemental information with 36 figures, and 8 tables and can be found online.

ACKNOWLEDGMENTS

H.F. acknowledges financial support from the National Natural Science Foundation of China (Grant No. 51902099), Hunan high-level talent gathering project (Grant No. 2019RS1021), Fundamental Research Funds for the Central Universities (Grant No. 531119200087) and the Innovative Research Groups of Hunan Province (Grant No. 2020JJ1001). G.Y. acknowledges support from the Hunan Province Natural Science Foundation (Grant No. 2020JJ4204). J.D. acknowledges support from Youth Innovation Promotion Association CAS. We thank Diamond Light Source for access and support in use of the electron Physical Science Imaging Centre (Instrument E02, proposal number MG27260) that contributed to the results presented here. We thank T. H. for the help with DFT analysis.

AUTHOR CONTRIBUTIONS

H.F. proposed the research direction and guided the project. J.L., G.Y. and W.G designed and performed the experiments. Z.G., C.A., J.D., J.L. and H.G. analyzed and discussed the experimental results and drafted the manuscript. J. L., K. H., M.Y., R. L. and G.H. joined the discussion and provided helpful suggestions.

DECLARATION OF INTERESTS

The authors declare no competing interests.

REFERENCES*

1. Suntivich, J., Gasteiger, H.A., Yabuuchi, N., Nakanishi, H., Goodenough, J.B., and Shao-Horn, Y. (2011). Design principles for oxygen-reduction activity on perovskite oxide catalysts for fuel cells and metal-air batteries. Nat. Chem. *3*, 546-550.
2. Huang, X.Q., Zhao, Z.P., Cao, L., Chen, Y., Zhu, E.B., Lin, Z.Y., Li, M.F., Yan, A.M., Zettl, A., Wang, Y.M., Duan, X.F., Mueller, T. and Huang, Y. (2015). High-performance transition metal-doped Pt_3Ni octahedra for oxygen reduction reaction. Science *348*, 1230-1234.
3. Wu, H.H., Li, H.B., Zhao, X.F., Liu, Q.F., Wang, J., Xiao, J.P., Xie, S.H., Si, R., Yang, F., Miao, S., Guo, X.G., Wang, G.X., and Bao, X.H. (2016). Highly doped and exposed Cu(I)-N active sites within graphene towards efficient oxygen reduction. Chem. Rev. *118*, 2302-2312.
4. Kulkarni, A., Siahrostami, S., Patel, A.J., and Nørskov, J.K. (2018). Understanding catalytic activity trends in the oxygen reduction reaction. Chem. Rev. *118*, 2302-2312.
5. He, Y.H., Liu, S.W., Priest, C., Shi, Q.R., and Wu, G. (2020). Atomically dispersed metal-nitrogen-carbon catalysts for fuel cells: advances in catalyst design, electrode performance, and durability improvement. Chem. Soc. Rev. *49*, 3484-3524.
6. Lu, X.F., Xia, B.Y., Zang, S.Q., and Lou, X.W. (2020). Metal-organic frameworks based electrocatalysts for the oxygen reduction reaction. Angew. Chem. Int. Ed. *59*, 4634-4650.
7. Yang, G.G., Zhu, J.W., Yuan, P.F., Hu, Y.F., Qu, G., Lu, B.A., Xue, X.Y., Yin, H.B., Cheng, W.Z., Cheng, J.Q., Xu, W.X., Li, J., Hu, J.S., Mu, S.C. and Zhang, J.N. (2021). Regulating Fe-spin state by atomically dispersed Mn-N in Fe-N-C catalysts with high oxygen reduction activity. Nat. Commun. *12*, 1734.

8. Wang, X.Q., Li, Z.J., Qu, Y.T., Yuan, T.W., Wang, W.Y., Wu, Y.E., and Li, Y.D. (2019). Review of metal catalysts for oxygen reduction reaction: from nanoscale engineering to atomic design. Chem. *5*, 1486-1511.
9. Liu, J., Jiao, M.G., Mei, B.B., Tong, Y.X., Li, Y.P., Ruan, M.B., Song, P., Sun, G.Q., Jiang, L.H., Wang, Y., Jiang, Z., Gu, L., Zhou, Z., and Xu, W.L. (2019). Carbon-supported divacancy-anchored platinum single-atom electrocatalysts with superhigh Pt utilization for the oxygen reduction reaction. Angew. Chem. Int. Ed. *58*, 1163-1167.
10. Qiao, B.T., Wang, A.Q., Yang, X.F., Allard, L.F., Jiang, Z., Cui, Y.T., Liu, J.Y., Li, J., and Zhang, T. (2011). Single-atom catalysis of CO oxidation using Pt_1/FeO_x. Nat. Chem. *3*, 634-641.
11. Fei, H.L, Dong, J.C., Arellano-Jimenez, M.J., Ye, G.L., Dong Kim, N., Samuel, E.L.G., Peng, Z.W., Zhu, Z., Qin, F., Bao, J.J., Yacaman M.J., Aiayan, P. M., Chen, D.L. and Tour, J.M. (2015). Atomic cobalt on nitrogen-doped graphene for hydrogen generation. Nat. Commun. *6*, 8668.
12. Fei, H.L., Dong, J.C., Feng, Y.X., Allen, C.S., Wan, C.Z., Volosskiy, B., Li, M.F., Zhao, Z.P., Wang, Y.L., Sun, H.T., An, P.F., Chen, W.X., Guo, Z.Y., Lee, C., Chen, D.L., Shakir, I., Liu, M.J., Hu, T.D., Li, Y.D., Kirkland, A.I., Duan, X.F. and Huang, Y. (2018). General synthesis and definitive structural identification of MN_4C_4 single-atom catalysts with tunable electrocatalytic activities. Nat. Catal. *1*, 63-72.
13. Fei, H.L., Dong, J.C., Chen, D.L., Hu, T.D., Duan, X.D., Shakir, I., Huang, Y., and Duan, X. F. (2019). Single atom electrocatalysts supported on graphene or graphene-like carbons. Chem. Soc. Rev. *48*, 5207-5241.
14. Tang, C., Chen, L., Li, H.J., Li, L.Q., Jiao, Y., Zheng, Y., Xu, H.L., Davey, K., and Qiao, S.Z. (2021). Tailoring acidic oxygen reduction selectivity on single-atom catalysts via modification of first and second coordination spheres. J. Am. Chem. Soc. *143*, 7819-7827.
15. Chen, Y.J., Ji, S.F., Chen, C., Peng, Q., Wang, D.S., and Li, Y.D. (2018). Single-atom catalysts: synthetic strategies and electrochemical applications. Joule *2*, 1242-1264.
16. Wan, X., Liu, X.F., Li, Y.C., Yu, R.H., Zheng, L.R., Yan, W.S., Wang, H., Xu, M., and Shui, J.L. (2019). Fe-N-C electrocatalyst with dense active sites and efficient mass transport for high-performance proton exchange membrane fuel cells. Nat. Catal. *2*, 259-268.
17. Chen, G.B., Liu, P., Liao, Z.Q., Sun, F.F., He, Y.H., Zhong, H.X., Zhang, T., Zschech, E., Chen, M.W., Wu, G., Zhang, J. and Feng, X. L. (2020). Zinc-mediated template synthesis of Fe-N-C electrocatalysts with densely accessible $Fe-N_x$ active sites for efficient oxygen reduction. Adv. Mater. *32*, 1907399.
18. Qiao, M.F., Wang, Y., Wang, Q., Hu, G.Z., Mamat, X., Zhang, S.S., and Wang, S.Y. (2020). Hierarchically ordered porous carbon with atomically dispersed FeN_4 for ultraefficient oxygen reduction reaction in proton-exchange membrane fuel cells. Angew. Chem. Int. Ed. *59*, 2688-2694.
19. Ao, X., Zhang, W., Zhao, B.T., Ding, Y., Nam, G., Soule, L., Abdelhafiz, A., Wang, C.D., and Liu, M.L. (2020). Atomically dispersed Fe-N-C decorated with Pt-alloy core-shell nanoparticles for improved activity and durability towards oxygen reduction. Energy Environ. Sci. *13*, 3032-3040.
20. Zhang, Z.P., Sun, J.T., Wang, F., and Dai, L.M. (2018). Efficient oxygen reduction reaction (ORR) catalysts based on single iron atoms dispersed on a hierarchically structured porous carbon framework. Angew. Chem. Int. Ed. *57*, 9038-9043.
21. Wang, M.G., Yang, W.J., Li, X.Z., Xu, Y.S., Zheng, L.R., Su, C.L., and Liu, B. (2021). Atomically dispersed Fe-heteroatom (N, S) bridge sites anchored on carbon nanosheets for promoting oxygen reduction reaction. ACS Energy Lett. *6*, 379-386.
22. Chen, Y.J., Ji, S.F., Zhao, S., Chen, W.X., Dong, J.C., Cheong, W.C., Shen, R.G., Wen, X.D., Zheng, L.R., Rykov, A.I., Cai, S.C., Tang, H.L., Zhuang, Z.B., Chen, C.,Peng, Q., Wang, D.S. (2018). Enhanced oxygen reduction with single-atomic-site iron catalysts for a zinc-air battery and hydrogen-air fuel cell. Nat. Commun. *9*, 5422.
23. Jiao, L., Zhang, R., Wan, G., Yang, W., Wan, X., Zhou, H., Shui, J.L., Yu, S.H., and Jiang, H.L. (2020). Nanocasting SiO_2 into metal-organic frameworks imparts dual protection to high-loading Fe single-atom electrocatalysts. Nat. Commun. *11*, 2831.
24. Zhou, Y.Y., Tao, X.F., Chen, G.B., Lu, R.H., Wang, D., Chen, M.X., Jin, E.Q., Yang, J., Liang, H.W., Zhao, Y., Feng, X.L., Nartia, A. and Müllen, K. (2020). Multilayer stabilization for fabricating high-loading single-atom catalysts. Nat. Commun. *11*, 5892.
25. Malko, D., Kucernak, A., and Lopes, T. (2016). In situ electrochemical quantification of active sites in Fe-N/C non-precious metal catalysts. Nat. Commun. *7*, 13285.
26. Hou, C.C., Zou, L.L., Sun, L.M., Zhang, K.X., Liu, Z., Li, Y.W., Li, C.X., Zou, R.Q., Yu, J.H., and Xu, Q. (2020). Single-atom iron catalysts on overhang-eave carbon cages for high-performance oxygen reduction reaction. Angew. Chem. Int. Ed. *59*, 7384-7389.

27. Lee, S.H., Kim, J., Chung, D.Y., Yoo, J.M., Lee, H.S., Kim, M.J., Mun, B.S., Kwon, S.G., Sung, Y.E., and Hyeon, T. (2019). Design principle of Fe-N-C electrocatalysts: how to optimize multimodal porous structures? J. Am. Chem. Soc. *141*, 2035-2045.
28. Tang, C., Wang, H.F., and Zhang, Q. (2018). Multiscale principles to boost reactivity in gas-involving energy electrocatalysis. Acc. Chem. Res. *51*, 881-889.
29. Sievers, G.W., Jensen, A.W., Quinson, J., Zana, A., Bizzotto, F., Oezaslan, M., Dworzak, A., Kirkensgaard, J.J.K., Smitshuysen, T.E.L., Kadkhodazadeh, S., Juelsholt, M., Jensen, K.M. Ø., Anklam, K., Wan, H., Schäfer, J., Čépe, K., Escudero-Escribano, M., Rossmeisl, J., Quade, A., Brüser, V., Arenz, M. (2021). Self-supported Pt-CoO networks combining high specific activity with high surface area for oxygen reduction. Nat. Mater. *20*, 208-213.
30. Ott, S., Orfanidi, A., Schmies, H., Anke, B., Nong, H.N., Hübner, J., Gernert, U., Gliech, M., Lerch, M., and Strasser, P. (2020). Ionomer distribution control in porous carbon-supported catalyst layers for high-power and low Pt-loaded proton exchange membrane fuel cells. Nat. Mater. *19*, 77-85.
31. Jiang, R., Li, L., Sheng, T., Hu, G.F., Chen, Y.G., and Wang, L.Y. (2018). Edge-site engineering of atomically dispersed Fe-N_4 by selective C-N bond cleavage for enhanced oxygen reduction reaction activities. J. Am. Chem. Soc. *140*, 11594-11598.
32. Xiao, M.L., Xing, Z.H., Jin, Z., Liu, C.P., Ge, J.J., Zhu, J.B., Wang, Y., Zhao, X., and Chen, Z.W. (2020). Preferentially engineering FeN_4 edge sites onto graphitic nanosheets for highly active and durable oxygen electrocatalysis in rechargeable Zn-air batteries. Adv. Mater. *32*, 2004900.
33. Wang, X., Jia, Y., Mao, X., Liu, D.B., He, W.X., Li, J., Liu, J.G., Yan, X.C., Chen, J., Song, L., Du, A.J., and Yao, X.D. (2020). Edge-rich Fe-N_4 active sites in defective carbon for oxygen reduction catalysis. Adv. Mater. *32*, 2000966.
34. Fu, X.G., Li, N., Ren, B.H., Jiang, G.P., Liu, Y.R., Hassan, F.M., Su, D., Zhu, J.B., Yang, L., Bai, Z.Y., Cano, Z.P., Yu, A.P., and Chen, Z.W. (2019). Tailoring FeN_4 sites with edge enrichment for boosted oxygen reduction performance in proton exchange membrane fuel cell. Adv. Energy Mater. *9*, 1803737.
35. Zhao, X.J., Pachfule, P., Li, S., Langenhahn, T., Ye, M.Y., Schlesiger, C., Praetz, S., Schmidt, J., and Thomas, A. (2019). Macro/microporous covalent organic frameworks for efficient electrocatalysis. J. Am. Chem. Soc. *141*, 6623-6630.
36. He, Y.H., Hwang, S., Cullen, D.A., Uddin, M.A., Langhorst, L., Li, B.Y., Karakalos, S., Kropf, A.J., Wegener, E.C., Sokolowski, J., Chen, M.J., Mayers, D., Su, D., More, K.L., Wang, G. F., Litster, S., and Wu, G. (2019). Highly active atomically dispersed CoN_4 fuel cell cathode catalysts derived from surfactant-assisted MOFs: carbon-shell confinement strategy. Energy Environ. Sci. *12*, 250-260.
37. Xia, W., Tang, J., Li, J.J., Zhang, S.H., Wu, K.C.W., He, J.P., and Yamauchi, Y. (2019). Defect-rich graphene nanomesh produced by thermal exfoliation of metal-organic frameworks for the oxygen reduction reaction. Angew. Chem. Int. Ed. *58*, 13354-13359.
38. Liang, J., Jiao, Y., Jaroniec, M., and Qiao, S.Z. (2012). Sulfur and nitrogen dual-doped mesoporous graphene electrocatalyst for oxygen reduction with synergistically enhanced performance. Angew. Chem. Int. Ed. *51*, 11496-11500.
39. Liu, J.J., He, T., Wang, Q.C., Zhou, Z.X., Zhang, Y.Q., Wu, H.Q., Li, Q., Zheng, J., Sun, Z.F., Lei, Y.P., Ma, J. M., and Zhang, Y. (2019). Confining ultrasmall bimetallic alloys in porous N-carbon for use as scalable and sustainable electrocatalysts for rechargeable Zn-air batteries. J. Mater. Chem. A. *7*, 12451-12456.
40. Tavakkoli, M., Flahaut, E., Peljo, P., Sainio, J., Davodi, F., Lobiak, E.V., Mustonen, K., and Kauppinen, E.I. (2020). Mesoporous single-atom-doped graphene-carbon nanotube hybrid: synthesis and tunable electrocatalytic activity for oxygen evolution and reduction reactions. ACS Catal. *10*, 4647-4658.
41. Jia, Y., Zhang, L.Z., Zhuang, L.Z., Liu, H.L., Yan, X.C., Wang, X., Liu, J.D., Wang, J.C., Zheng, Y.R., Xiao, Z.H., Taran, E., Chen, J., Yang, D.J., Zhu, Z.H., Wang, S.Y., Dai, L.M., and Yao, X.D. (2019). Identification of active sites for acidic oxygen reduction on carbon catalysts with and without nitrogen doping. Nat. Catal. *2*, 688-695.
42. Li, J., Chen, S.G., Yang, N., Deng, M.M., Ibraheem, S., Deng, J.H., Li, J., Li, L., and Wei, Z.D. (2019). Ultrahigh-loading zinc single-atom catalyst for highly efficient oxygen reduction in both acidic and akaline media. Angew. Chem. Int. Ed. *58*, 7035-7039.
43. Zhang, N., Zhou, T.P., Chen, M.L., Feng, H., Yuan, R.L., Zhong, C.A., Yan, W.S., Tian, Y.C., Wu, X.J., Chu, W.S., Wu, C.Z. and Xie, Y. (2020). High-purity pyrrole-type FeN_4 sites as a superior oxygen reduction electrocatalyst. Energy Environ. Sci. *13*, 111-118.
44. Zhang, X.Y., Zhang, S., Yang, Y., Wang, L.G., Mu, Z.J., Zhu, H.S., Zhu, X.Q., Xing, H.H., Xia, H.Y., Huang, B.L., Li, J., Guo, S.J., and Wang, E.K. (2020). A general method for transition

metal single atoms anchored on honeycomb-like nitrogen-doped carbon nanosheets. Adv. Mater. *32*, 1906905.
45. Wang, T.T., Sang, X.H., Zheng, W.Z., Yang, B., Yao, S., Lei, C.J., Li, Z.J., He, Q.G., Lu, J.G., Lei, L.C., Dai, L.M., and Hou, Y. (2020). Gas diffusion strategy for inserting atomic iron sites into graphitized carbon supports for unusually high-efficient CO_2 electroreduction and high-performance Zn-CO_2 batteries. Adv. Mater. *32*, 2002430.
46. McCrory, C.C.L., Jung, S., Peters, J.C., and Jaramillo, T.F. (2013). Benchmarking heterogeneous electrocatalysts for the oxygen evolution reaction. J. Am. Chem. Soc. *135*, 16977-16987.
47. Pan, F.P., Li, B.Y., Sarnello, E., Fei, Y.H., Feng, X.H., Gang, Y., Xiang, X.M., Fang, L.Z., Li, T., Hu, Y.H., Wang, G.F., and Li, Y. (2020). Pore-edge tailoring of single-atom iron-nitrogen sites on graphene for enhanced CO_2 reduction. ACS Catal. *10*, 10803-10811.
48. Primbs, M., Sun, Y.Y., Roy, A., Malko, D., Mehmood, A., Sougrati, M.T., Blanchard, P.Y., Granozzi, G., Kosmala, T., Daniel, G., Atanassov, P., Sharman, J., Durante, C., Kucernak, A., Jones, D., Jaouen, F., and Strasser, P. (2020). Establishing reactivity descriptors for platinum group metal (PGM)-free Fe-N-C catalysts for PEM fuel cells. Energy Environ. Sci. *13*, 2480-2500.
49. Luo, F., Wagner, S., Onishi, I., Selve, S., Li, S., Ju, W., Wang, H., Steinberg, J., Thomas, A., Kramm, U.I., and Strasser, P. (2021). Surface site density and utilization of platinum group metal (PGM)-free Fe-NC and FeNi-NC electrocatalysts for the oxygen reduction reaction. Chem. Sci. *12*, 384-396.
50. Diao, J.X., Qiu, Y., Liu, S.Q., Wang, W.T., Chen, K., Li, H.L., Yuan, W.Y., Qu, Y.T., and Guo, X.H. (2020). Interfacial engineering of W_2N/WC heterostructures derived from solid-state synthesis: a highly eficient trifunctional electrocatalyst for ORR, OER, and HER. Adv. Mater. *32*, 1905679.
51. Inaba, M., Jensen, A.W., Sievers, G.W., Escudero-Escribano, M., Zana, A., and Arenz, M. (2018). Benchmarking high surface area electrocatalysts in a gas diffusion electrode: measurement of oxygen reduction activities under realistic conditions. Energy Environ. Sci. *11*, 988-994.
52. Ehelebe, K., Seebergr, D., Paul, M.T.Y., Thiele, S., Mayrhofer, K.J.J., and Cherevko, S. (2019). Evaluating electrocatalysts at relevant currents in a half-cell: the impact of Pt loading on oxygen reduction reaction. J. Electrochem. Soc. *166*, 1259-1268.
53. Antonacci, P., Chevalier, S., Lee, J., Ge, N., Hinebaugh, J., Yip, R., Tabuchi, Y., Kotaka, T., and Bazylak, A. (2016). Balancing mass transport resistance and membrane resistance when tailoring microporous layer thickness for polymer electrolyte membrane fuel cells operating at high current densities. Electrochim. Acta *188*, 888-897.
54. Higginbotham, A.L., Kosynkin, D.V., Sinitskii, A., Sun, Z., and Tour, J.M. (2010). Lower-Defect Graphene Oxide Nanoribbons from Multiwalled Carbon Nanotubes. ACS Nano *4*, 2059-2069.
55. Kresse, G., and Furthmuller, J. (1996). Efficiency of ab-initio total energy calculations for metals and semiconductors using a plane-wave basis set. Comput. Mater. Sci. *6*, 15-50.
56. Kresse, G., and Furthmuller, J. (1996). Efficient iterative schemes for ab initio total-energy calculations using a plane-wave basis set. Phys. Rev. B *54*, 11169-11186.
57. Perdew, J.P., Burke, K., and Ernzerhof, M. (1996). Generalized Gradient Approximation Made Simple. Phys. Rev. Lett. *77*, 3865-3868.
58. Monkhorst, H.J., and Pack, J.D. (1976). Special points for Brillouin-zone integrations. Phys. Rev. B *13*, 5188-5192.
59. Blochl, P.E. (1994). Projector augmented-wave method. Phys. Rev. B *50*, 17953-17979.
60. Rossmeisl, J., Logadottir, A., and Nørskov, J.K. (2005). Electrolysis of water on (oxidized) metal surfaces. Chem. Phys. *319*, 178-184.
61. Grimme, S., Antony, J., Ehrlich, S., and Krieg, H. (2010). A consistent and accurate ab initio parametrization of density functional dispersion correction (DFT-D) for the 94 elements H-Pu. J. Chem. Phys. *132*, 154104.
62. Peterson, A.A., Abild-Pedersen, F., Studt, F., Rossmeisl, J., and Nørskov, J.K. (2010). How copper catalyzes the electroreduction of carbon dioxide into hydrocarbon fuels. Energy Environ. Sci. *3*, 1311-1315.